

Automated Temperature and Emission Measure Analysis of Coronal Loops and Active Regions Observed with the Atmospheric Imaging Assembly on the Solar Dynamics Observatory (SDO/AIA)

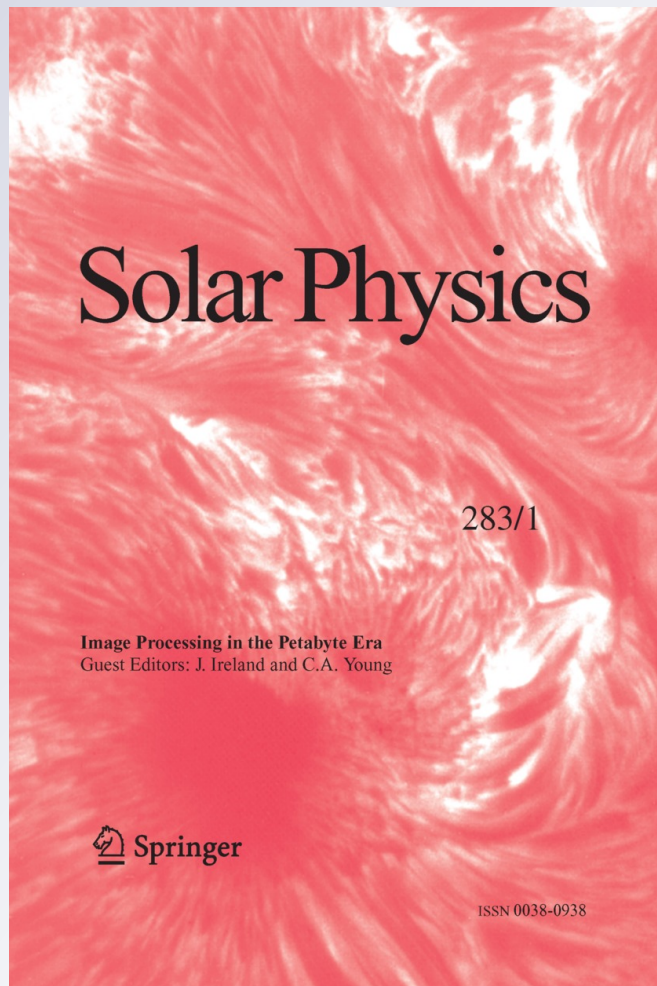
Markus J. Aschwanden, Paul Boerner, Carolus J. Schrijver & Anna Malanushenko

Solar Physics

A Journal for Solar and Solar-Stellar Research and the Study of Solar Terrestrial Physics

ISSN 0038-0938
Volume 283
Number 1

Sol Phys (2013) 283:5–30
DOI 10.1007/s11207-011-9876-5



Your article is protected by copyright and all rights are held exclusively by Springer Science+Business Media B.V.. This e-offprint is for personal use only and shall not be self-archived in electronic repositories. If you wish to self-archive your work, please use the accepted author's version for posting to your own website or your institution's repository. You may further deposit the accepted author's version on a funder's repository at a funder's request, provided it is not made publicly available until 12 months after publication.

Automated Temperature and Emission Measure Analysis of Coronal Loops and Active Regions Observed with the Atmospheric Imaging Assembly on the Solar Dynamics Observatory (SDO/AIA)

Markus J. Aschwanden · Paul Boerner ·
Carolan J. Schrijver · Anna Malanushenko

Received: 21 March 2011 / Accepted: 10 October 2011 / Published online: 15 November 2011
© Springer Science+Business Media B.V. 2011

Abstract We developed numerical codes designed for automated analysis of SDO/AIA image datasets in the six coronal filters, including: *i*) coalignment test between different wavelengths with measurements of the altitude of the EUV-absorbing chromosphere, *ii*) self-calibration by empirical correction of instrumental response functions, *iii*) automated generation of differential emission measure [DEM] distributions with peak-temperature maps [$T_p(x, y)$] and emission measure maps [$EM_p(x, y)$] of the full Sun or active region areas, *iv*) composite DEM distributions [$dEM(T)/dT$] of active regions or subareas, *v*) automated detection of coronal loops, and *vi*) automated background subtraction and thermal analysis of coronal loops, which yields statistics of loop temperatures [T_e], temperature widths [σ_T], emission measures [EM], electron densities [n_e], and loop widths [w]. The combination of these numerical codes allows for automated and objective processing of numerous coronal loops. As an example, we present the results of an application to the active region NOAA 11158, observed on 15 February 2011, shortly before it produced the largest (X2.2) flare during the current solar cycle. We detect 570 loop segments at temperatures in the entire range of $\log(T_e) = 5.7 - 7.0$ K and corroborate previous TRACE and AIA results on their near-isothermality and the validity of the Rosner–Tucker–Vaiana (RTV) law at soft X-ray temperatures ($T \gtrsim 2$ MK) and its failure at lower EUV temperatures.

Keywords Sun: corona · Thermal analysis · Differential emission measure analysis · Methods

1. Introduction

Isaac Asimov anticipated the inescapable data-analysis dilemma of the *Solar Dynamics Observatory* (SDO) when he said: “I do not fear computers. I fear the lack of them.” We may

Image Processing in the Petabyte Era
Guest Editors: J. Ireland and C.A. Young

M.J. Aschwanden (✉) · P. Boerner · C.J. Schrijver · A. Malanushenko
Solar and Astrophysics Laboratory, Dept. ADBS, Lockheed Martin Advanced Technology Center,
Bldg. 252, 3251 Hanover St., Palo Alto, CA 94304, USA
e-mail: aschwanden@lmsal.com

add that solar image processing in the petabyte era would be so inefficient on a manual basis that we solar physicists would be judged as highly irresponsible and oblivious in dealing with the gold mine of data that SDO provides. The push for fully automated data-analysis tools, which cannot be substituted by manual or visual methods, is thus motivated by a host of reasons: *i*) automated identification and classification of solar phenomena; *ii*) automated localization and time tracking of phenomena; *iii*) efficiency of data selection, data mining, and standard data-analysis tasks; *iv*) large statistics of observables; *v*) objectivity of data analysis; *vi*) efficient visualization of imagery and movies; and *vii*) prompt real-time prediction of dynamic solar phenomena. For a recent review of image processing techniques and feature recognition in solar physics see Aschwanden (2010a) and related articles in the same Topical Issue **262/2** of *Solar Physics* (Ireland and Young, 2010).

In this article we describe a number of new data-analysis tools designed for automated application to *Atmospheric Imaging Assembly* (AIA) data, recorded in six coronal temperature wavelength filters, which are made publicly available in the Solar Software (SSW) package. These automated data-analysis tools are designed to retrieve physical parameters from the observed multiwavelength fluxes, such as differential emission measure [DEM] distributions, electron temperatures, and electron densities, for solar active regions and coronal loops, as well as some geometric parameters of coronal loops. Methods to determine DEM distributions of solar coronal plasma have been pioneered with regularization and maximum entropy methods (*e.g.*, Fludra and Sylwester, 1986), iterative fitting with cubic spline functions (*e.g.*, Brosius *et al.*, 1996), with a Markov chain Monte Carlo approach (*e.g.*, Kashyap and Drake, 1998), or with forward fitting of single Gaussian functions in the case of triple-filter data (*e.g.*, Aschwanden and Acton, 2001; Aschwanden and Nightingale, 2005), or multi-Gaussian functions in the case of six-filter data (Aschwanden and Boerner, 2011).

In this article we automate the forward fitting of single-Gaussian DEM distributions on a pixel-by-pixel basis, which can then be synthesized to more complex DEM distribution functions by summing the single-pixel DEMs over arbitrary larger areas. We combine here also, for the first time, an automated loop-detection code (Aschwanden, 2010a, 2010b) with coronal loop thermal analysis (Aschwanden and Boerner, 2011), which eliminates any human bias resulting from individual loop selections or background choices, and thus should warrant more objective and statistically representative results. Besides the obvious benefits of high numerical efficiency, large statistics, and objectivity of the data analysis, applying these automated AIA analysis tools also provides other benefits, such as self-calibration of the instrumental response functions and tests of theoretical scaling laws.

2. Automated Data Analysis

In the following subsections we describe automated AIA analysis tools and results stepwise in order of numerical necessity and increasing complexity of tasks. The described tasks can be implemented in an automated analysis run in the same logical order.

2.1. Instrument

The *Atmospheric Imaging Assembly* (AIA) instrument onboard the *Solar Dynamics Observatory* (SDO) started observations on 29 March 2010; since then it has produced essentially continuous data of the full Sun with four 4096×4096 detectors with a pixel size of $0.6''$, corresponding to an effective spatial resolution of $\approx 1.6''$. AIA contains ten different wavelength

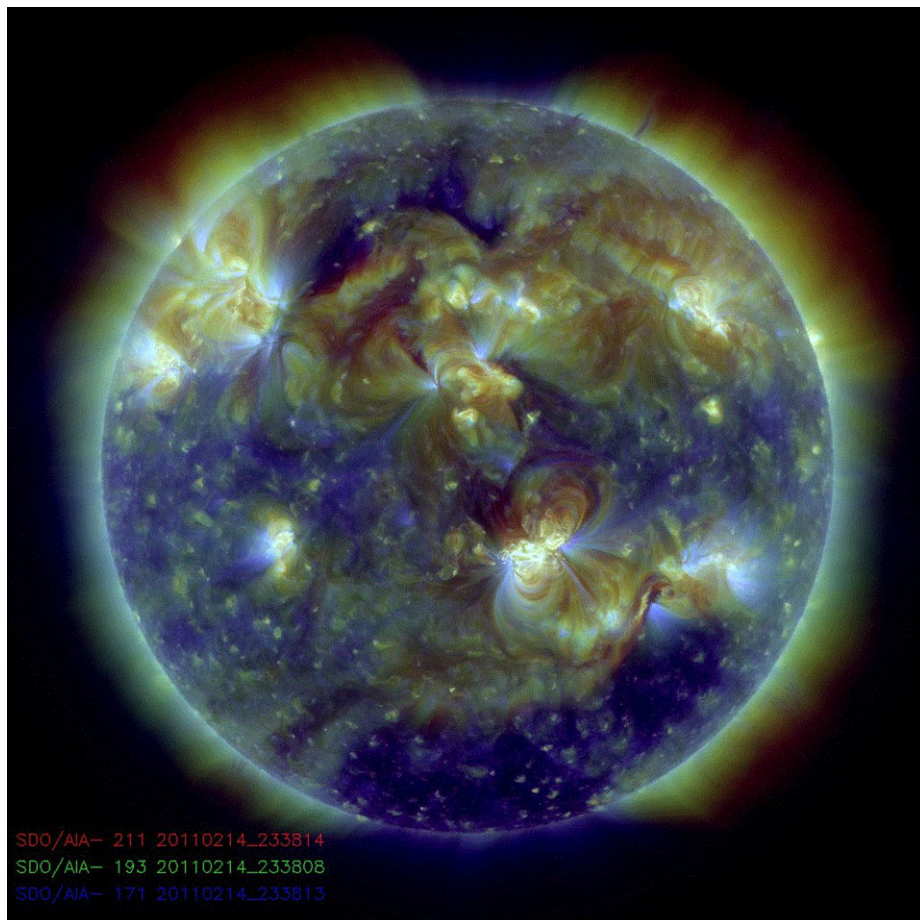


Figure 1 Composite triple-filter image of SDO/AIA consisting of a 211 Å (red), 193 Å (green), and 171 Å (blue) image, recorded on 14 February 2011 at 23:38 UT [courtesy of AIA team].

channels, three in white light and UV, and seven EUV channels, whereof six wavelengths (131, 171, 193, 211, 335, 94 Å) are centered on strong iron lines (Fe VIII, IX, XII, XIV, XVI, XVIII), covering the coronal range from $T \approx 0.6$ MK to $\gtrsim 16$ MK. AIA records a full set of near-simultaneous images in each temperature filter with a fixed cadence of currently 12 seconds. Instrumental descriptions can be found in Lemen *et al.* (2011) and Boerner *et al.* (2011).

2.2. Observations

For our demonstration of data-analysis tools we select observations from a day that was rich in active regions and flare activity, namely 15 February 2011. This was the day when the first X-class flare of Solar Cycle 24 occurred, a *Geostationary Operational Environmental Satellite* (GOES)-class X2.2 event at 01:45 UT in NOAA active region 11158. Figure 1 shows a three-filter composite AIA image (211, 193, 171 Å) at 14 February 2011 at 23:38 UT. There are at least six active regions present on the disk, four in the northern hemisphere

and two in the southern hemisphere, with the flare-producing active region NOAA 11158 located in the southwest quadrant.

For the following tasks we choose the first image set of the day (15 February 2011), which was taken during the first 12 seconds after midnight, in the order of 171, 211, 94, 335, 193, 131 Å at 1, 2, 3, 5, 8, and 11 seconds after 00:00:00 UT.

2.3. Coalignment Test and Chromospheric Height Measurements

A first requirement for multiwavelength studies is a perfect (say a half pixel) coalignment between the images in different wavelengths. The coalignment of AIA images in the six coronal EUV wavelengths is carried out by limb fits and is incorporated in the Flexible Image Transport System (FITS) headers (in the keywords CRPIX1, CRPIX2 that give the pixel number of the Sun center, and RSUN_OBS, DSUN_OBS, and CDELT1, which give the solar radius, solar distance, and the plate scale). The currently reprocessed level 1.5 AIA images have a relative coalignment accuracy of $\lesssim 1$ pixel, although there are some daily variations in the order of ≈ 0.5 pixel due to temperature effects on the telescope induced by the Earth's albedo (R.A. Shine, private communication, 2011).

The solar limb in EUV images typically appears a few thousand kilometers higher than the photospheric altitude level, due to occultation of the bright coronal background by the optically thick chromosphere, which amounts to about five–ten AIA pixels. We can verify the coalignment accuracy by fitting the EUV limb and verifying the symmetry of the EUV limb offset with respect to the optical limb in the East–West (E–W) and North–South (N–S) directions, which is shown in Figure 2. We determine the average radial EUV flux profiles [$I_\lambda(r)$] at four positions (east and west limbs, South and North Poles) and define the height [h_λ] of the EUV chromosphere in each wavelength by the offset of the location with the steepest flux gradient (supposedly at the top of the chromosphere) from the optical solar radius [r_\odot] (dashed line in Figure 2),

$$h_\lambda = r_\lambda - r_\odot. \quad (1)$$

The so-defined heights of the chromosphere in each wavelength are given in Figure 2. Averaging the chromospheric heights from the four positions, we obtain the following mean values in each wavelength:

$$\begin{aligned} h_{131} &= 2700 \pm 400 \text{ km}, \\ h_{171} &= 3400 \pm 400 \text{ km}, \\ h_{193} &= 3700 \pm 700 \text{ km}, \\ h_{211} &= 3500 \pm 900 \text{ km}, \\ h_{335} &= 4200 \pm 1000 \text{ km}, \\ h_{94} &= 2500 \pm 500 \text{ km}. \end{aligned} \quad (2)$$

There seems to be a systematic dependence of the chromospheric height on the temperature, being lowest ($h \lesssim 3000$ km) for $T \leq 1.0$ MK (94 and 131 Å) and highest ($h \approx 3500$ –4000 km) for $T \geq 1.0$ MK (193, 211, 335 Å), which probably is a function of the absorption coefficient of the EUV continuum spectrum.

Assuming symmetric atmospheres at opposite sides of the Sun, we can test the coalignment accuracy by using the differences of chromospheric heights at opposite sides, for which

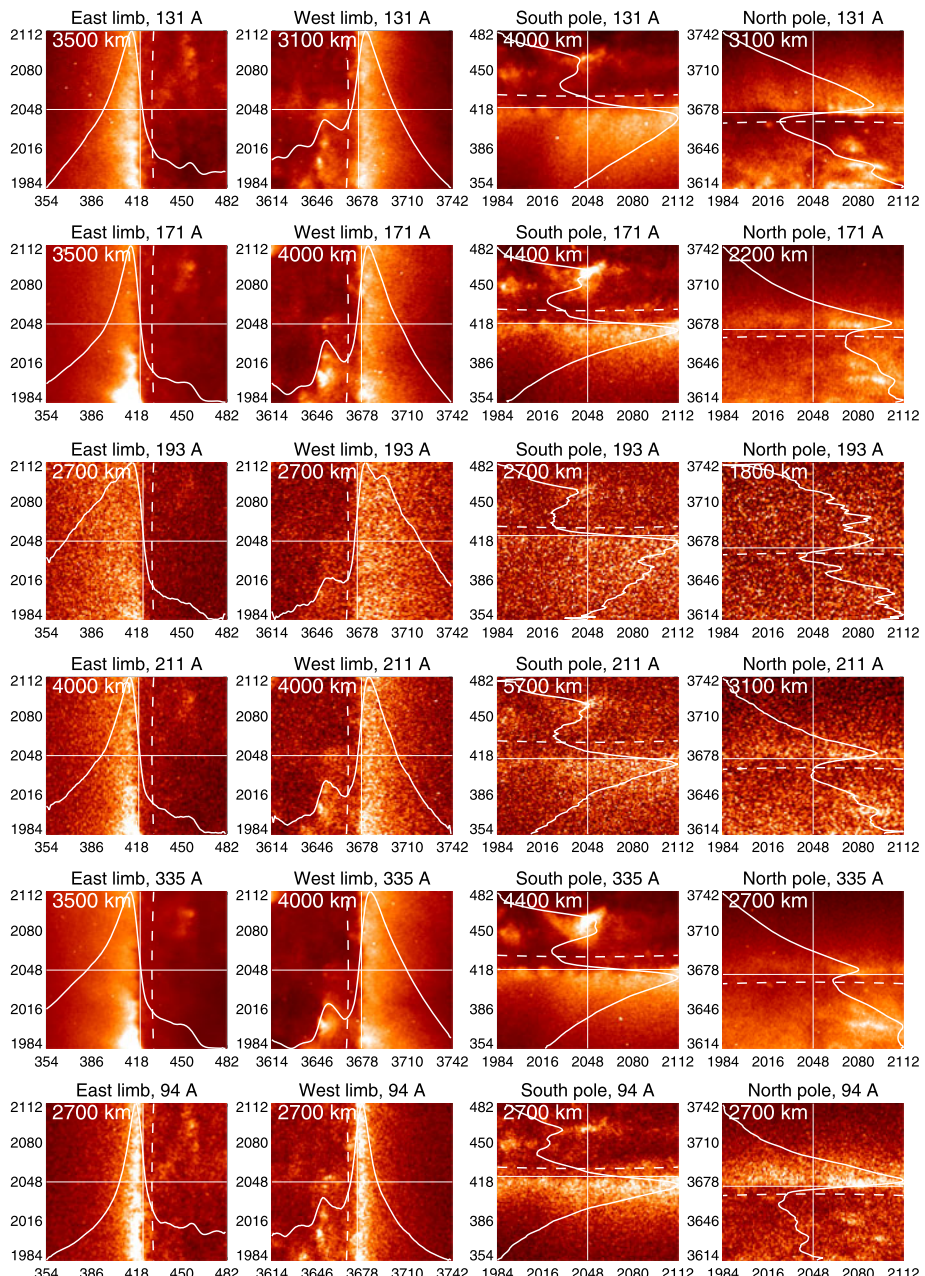


Figure 2 Coalignment test of image portions (with size 128×128) at the east limb (left column), west limb (second column), South Pole (third column), and North Pole (right column) for six coronal wavelengths (rows), overlaid with the average intensity profile $[I_\lambda(r)]$ in the radial direction (white curve), the EUV limb position (white crosshair), and the optical disk (dashed line). The altitude of the EUV chromosphere is measured with respect to the optical limb and is indicated in kilometers.

we find (averaged over the six wavelengths),

$$\begin{aligned}\langle \Delta x \rangle &= 0.8 \pm 0.5 \text{ pixels}, \\ \langle \Delta y \rangle &= 0.2 \pm 0.3 \text{ pixels}.\end{aligned}\quad (3)$$

The mean of the offset, 0.8 pixel in the E–W direction and 0.2 pixel in the N–S direction, is only important for absolute coalignment with other datasets, while the standard deviation of 0.5 pixel in the E–W direction and 0.3 pixel in the N–S direction yields an upper limit on the relative coalignment accuracy between the different wavelength filters. Part of the difference could be due to local deviations of the chromospheric height from the average value. For instance, the limb was higher at the poles than at the Equator for 304 Å images (Zhang, White, and Kundu, 1998). Therefore, our coalignment test for this dataset is consistent with the claimed accuracy of $\lesssim 1$ pixel between different wavelengths.

Cross-correlation of localized features in coronal wavelengths is not recommended due to the different temperatures and resulting morphological appearance of EUV features in each wavelength.

2.4. Automated Peak Emission Measure and Peak-Temperature Maps

AIA observes the Sun in six coronal temperature filters, and the images in each wavelength contain the EUV intensities [$F_\lambda(x, y)$] that emphasize those coronal features with temperatures near the peak sensitivity [T_λ] of the filter passband. A synthesized view of the six different filters can be conveyed by the differential emission measure [DEM] distribution [$dEM(T, x, y)/dT$], which can be reconstructed from the six filter fluxes [$F_\lambda(x, y)$] (in each pixel), defined as

$$F_\lambda(x, y) = \int \frac{dEM(T, x, y)}{dT} R_\lambda(T) dT, \quad (4)$$

where the flux [$F_\lambda(x, y)$] is defined in units of data numbers per second [DN s⁻¹ pixel⁻¹], $R_\lambda(T)$ are the filter response functions [in units of DN cm⁻⁵ s⁻¹ pixel⁻¹], and dEM/dT is the emission measure [in units of cm⁻⁵ K⁻¹]. For all DEM calculations in this article we use the empirically corrected response functions [$R(T)$] as derived in Section 2.5, with a correction factor of $q_{94} \approx 5$. One of the simplest representations of a DEM distribution is a Gaussian function

$$\frac{dEM(T, x, y)}{dT} = EM_p(x, y) \exp\left(-\frac{[\log(T) - \log(T_p(x, y))]^2}{2\sigma_T^2(x, y)}\right), \quad (5)$$

that can be characterized by the three parameters [EM_p , T_p , and σ_p] for each pixel position [(x, y)]. A single Gaussian function was found to fit background-subtracted coronal loops in 66% of the cases with a goodness of fit of $\chi^2 \leq 2$ (Aschwanden and Boerner, 2011). Even if a DEM is generally a more complicated function, it is useful to characterize it with the DEM peak emission measure value [EM_p] and DEM peak temperature [T_p], which can be achieved by a Gaussian fit. With this method we can produce an emission measure map [$EM_p(x, y)$] and a temperature map [$T_p(x, y)$], but we must keep in mind that the observed plasma is not necessarily isothermal for any position [x, y], but rather characterized by an *emission measure-weighted temperature*, for a given line of sight at position (x, y).

We developed an automated code to produce such emission-measure and temperature maps using the following simple algorithm. A filter-flux lookup table [$F^{\text{model}}(T_i, \sigma_j, \lambda_k)$] is precalculated for $n_T = 23$ temperature values T_i , $i = 1, \dots, n_T$ (equispaced in the logarithm

of the temperature between $\log(T) = 5.7$ and $\log(T) = 7.0$, for $n_\sigma = 10$ Gaussian temperature widths $\sigma_j = [0.1, 0.2, \dots, 1.0]$, and for the six filter wavelengths $\lambda_k, k = 1, \dots, 6$. The Gaussian DEM model fluxes [$F^{\text{model}}(T_i, \sigma_j, \lambda_k)$] are then forward-fitted to the observed fluxes [$F^{\text{obs}}(x, y)$] in each pixel position $[x, y]$ and the best-fit values [$EM_p(x, y)$, $T_p(x, y)$, and $\sigma_T(x, y)$] are then determined with the (reduced) least-square optimization criterion,

$$\chi^2(x, y) = \frac{1}{(n - n_{\text{free}})} \sum_k \frac{[F^{\text{obs}}(x, y, \lambda_k) - F^{\text{model}}(x, y, \lambda_k)]^2}{\sigma_F^2(x, y, \lambda_k)}, \quad (6)$$

where $n = 6$ is the number of observables at each position $[x, y]$, $n_{\text{free}} = 3$ is the number of free model parameters, and $\sigma_F(x, y, \lambda_k)$ is the expected uncertainty of an observed flux value [$F_\lambda(x, y)$] according to Poisson statistics,

$$\sigma_F(x, y, \lambda_k) = \frac{1}{\Delta t_{\text{exp}} N_{\text{obs}}^2} \sqrt{\sum_i^{N_{\text{obs}}} \sum_j^{N_{\text{obs}}} F_\lambda(x_i, y_j) t_{\text{exp}}}, \quad (7)$$

where $F_\lambda(x_i, y_j)$ is the intensity values per pixel normalized by the exposure time [t_{exp}] in units of DN s^{-1} . Thus, the Poisson statistics are corrected for the number of counts accumulated over the exposure time [t_{exp}] and combined macropixels with areas of N_{obs}^2 pixels. For accurate photon statistics, the number of photons is needed, rather than the data number. However, the data number is approximately equal to the photon number for the AIA EUV channels: $\text{DN photon}^{-1} \approx 0.9 - 1.5$ for the 131, 171, 195, 211 Å channels, $\text{DN photons}^{-1} \approx 0.6 - 0.7$ for the 304 and 335 Å channels, and $\text{DN photon}^{-1} \approx 2.1$ for the 94 Å channel (see Table 2 in Boerner *et al.*, 2011).

A temperature map [$T(x, y)$] obtained from the six AIA filter images recorded on 15 February 2011 at 00:00 UT is shown in Figure 3, covering the temperature range of $T = 0.5 - 10 \text{ MK}$ or $\log(T) = 5.7 - 7.0$, with the temperature scale shown as a vertical bar at the right side of the image. The temperature map shows the coolest temperature of $T \lesssim 10^{5.7} \approx 0.5 \text{ MK}$ in the southern coronal hole region, a slightly higher temperature of $T \approx 10^{6.1} \approx 1.2 \text{ MK}$ at the North Pole, $T \approx 10^{5.8} - 10^{6.2} \approx 0.6 - 1.5 \text{ MK}$ in quiet-Sun regions in the southern hemisphere, $T \approx 10^{6.2} - 10^{6.4} \approx 1.5 - 2.5 \text{ MK}$ in quiet-Sun regions in the northern hemisphere, and up to $T \lesssim 10^{7.0} \approx 10 \text{ MK}$ in the central active region (which produced the X2.2 flare 1.5 hours later).

A more detailed comparison between a cool-temperature filter (171 Å), a high-temperature filter (335 Å), a peak emission measure map [$EM_p(x, y)$], and a DEM peak-temperature map [$T_p(x, y)$] is shown in Figure 4. The active region NOAA 11158 Southwest of disk center clearly shows that the hottest zone is located in the core, while the cooler loops are situated at the periphery of the active region. The temperature map differentiates hot and cool structures better than do single filters. The DEM peak emission-measure map visualizes the sum of (squared) electron densities, or the total mass distribution, regardless of the temperature. Above the limb, the near-exponential drop-off of density with height can be seen both in the emission-measure map and in single filters, while the temperature map shows no decrease with altitude.

A distribution of peak emission measure values [EM_p] versus peak temperatures [T_p] is shown in Figure 5 in the form of a logarithmic contour plot. This distribution shows a tendency of $EM_p \propto T_p^4$ for hotter temperatures, which we will discuss in Section 2.11 in terms of loop scaling laws. The $EM_p - T_p$ distribution also exhibits a paramount maximum

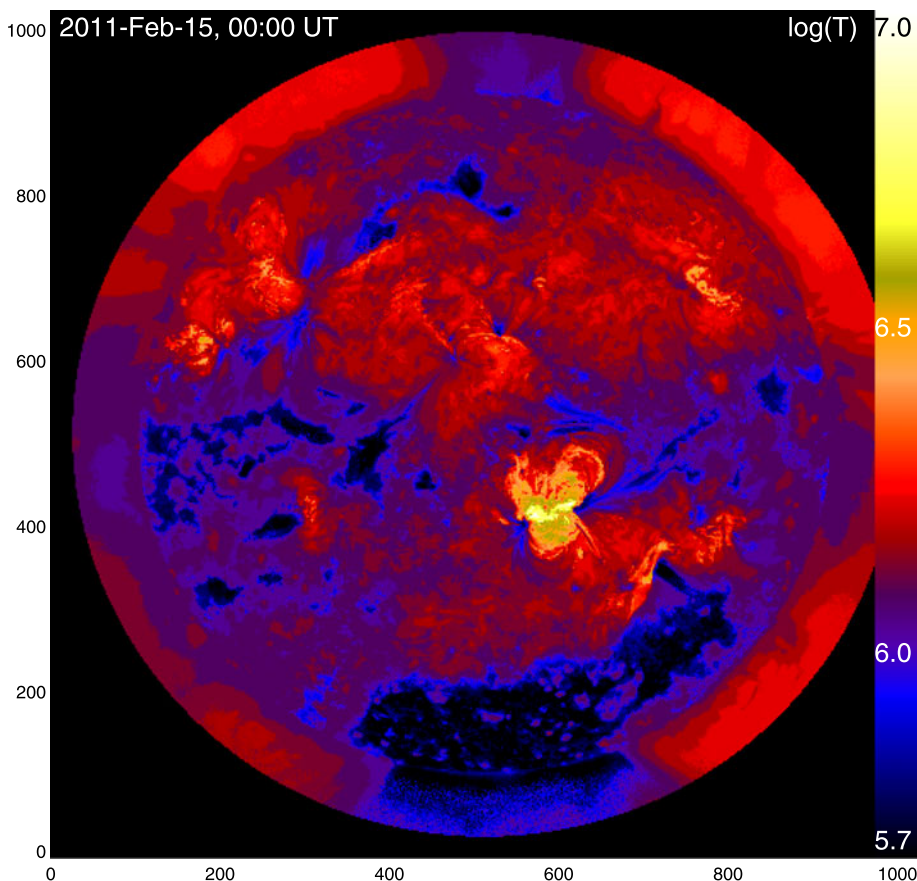


Figure 3 A temperature map calculated from the six AIA coronal filters recorded on 15 February 2011, at 00:00 UT. The temperature range is indicated in the vertical color bar on the right side, $\log(T) = 5.7 - 7.0$. The spatial resolution of the temperature map is $2.4''$, and each temperature value is calculated for an averaged macropixel with an area of 4×4 pixels.

of values in the temperature range of $\log(T) \approx 6.1 - 6.2$ ($T \approx 1.2 - 1.6$ MK). Apparently, the lifetime of coronal loops is longest at this temperature, while they rapidly decrease during the cooling phase below $T \lesssim 1.0$ MK. This may be a strong constraint for theoretical modeling of the energy balance and dynamics in coronal structures.

2.5. Empirical Correction of Instrumental Response Functions

The response functions of all AIA filters is available in the SolarSoft (SSW) software and documented on the SDO documentation web site <http://www.lmsal.com/sdodocs/> (see “Guide to SDO Data Analysis”). Another application of our automated DEM fitting is a self-calibration of the AIA response functions, based on the self-consistency of DEM fitting to many coronal structures. For instance, the nominal response function of the AIA 94 Å filter as available in the Solar Software (SSW) package (at the time of writing) is known to be incorrect, and a preliminary empirical correction was evaluated from 100 DEM fits to coronal loops by Aschwanden and Boerner (2011). The nominal 94 Å response function is

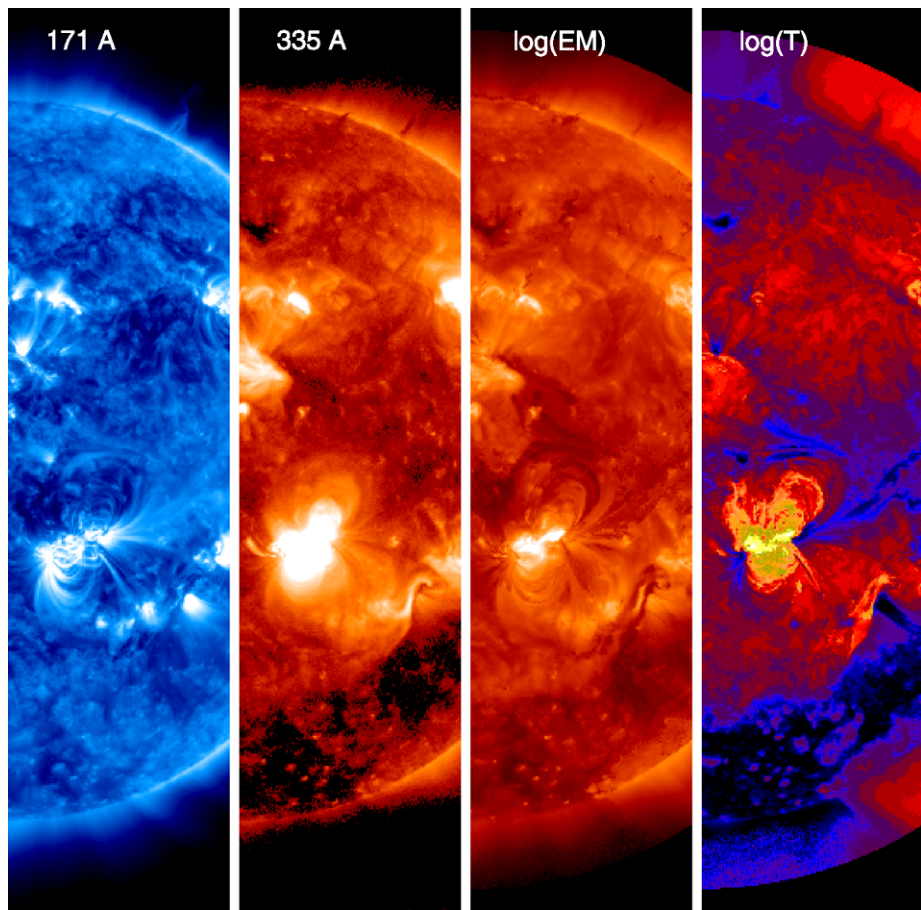


Figure 4 Comparison of partial image of the Sun in a cool-temperature filter (171 Å, left), a high-temperature filter (335 Å, second from left), the peak emission measure map [$EM_p(x, y)$] (second from right), and the DEM peak-temperature map [$T_p(x, y)$]. All images are displayed on a logarithmic scale.

shown in Figure 6, which shows a double peak at $\log(T) \approx 6.1$ due to Fe X lines and at $\log(T) \approx 6.8$ due to Fe XVIII lines. AIA images in 94 Å often display strong emission from the $\log(T) \approx 6.0$ quiet corona that is in excess of the expected response function. Therefore, one suspects that many Fe VIII, Fe IX, and Fe X atomic transitions are not included in the currently available CHIANTI code (H. Warren, P. Testa; private communication, 2011), which is the atomic database of the AIA response-function calculation.

In order to derive a first-order correction to the nominal 94 Å response function [$R_{94}(T)^{\text{nom}}$], we can define an empirical boost factor [q_{94}] for the cool-temperature peak of the 94 Å response function, say at $\log(T) \leq 6.3$ (Aschwanden and Boerner, 2011),

$$R_{94}(T)^{\text{emp}} = \begin{cases} q_{94} R_{94}(T)^{\text{nom}} & \text{for } \log(T) \leq 6.3 \text{ Å}, \\ R_{94}(T)^{\text{nom}} & \text{for } \log(T) > 6.3 \text{ Å}. \end{cases} \quad (8)$$

The nominal response function [$R_{94}(T)^{\text{nom}}$] corresponds to the AIA software that is currently available in SolarSoft (SSW) and is used here to evaluate the corrected re-

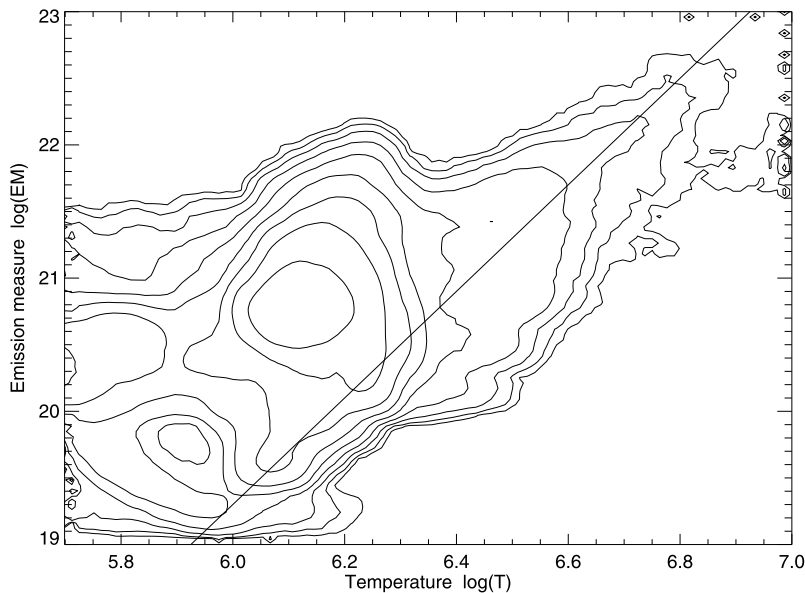


Figure 5 Emission measure vs. temperature map for the solar corona of 15 February 2011, 00:00 UT, shown as a contour plot with logarithmic contours with a dynamic range of 10^4 between the lowest and highest number of cases measured in each 4×4 macropixel. Overlayed is the RTV scaling law $EM \propto T^4$, which applies to the hotter temperature regime.

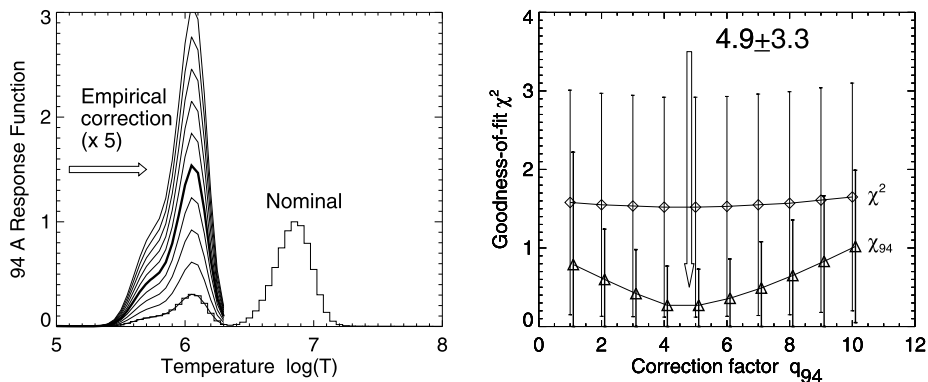


Figure 6 Empirical correction of AIA 94 Å response function for the low-temperature response at $\log(T) < 6.3$ (left panel), based on the goodness of fit of DEM forward fitting in $\approx 10^6$ macropixels, as depicted in Figure 3. The nominal response function is shown as a histogram. The overall goodness of fit in all six AIA channels is $\chi = 1.52 \pm 1.40$, and for the 94 Å channel $\chi_{94} = 0.27$ for the best-fit value of the correction factor $q_{94} = 4.9 \pm 3.3$.

sponse [$R_{94}(T)^{\text{emp}}$]. The change of the nominal response function for boost factors of $q_{94} = 1, \dots, 10$ is shown in Figure 6 (left panel). In the previous study (Aschwanden and Boerner, 2011), an empirical correction with the factor $q_{94} = 6.7 \pm 1.7$ was found. Here we run a sequence of DEM fits to the AIA images with a resolution of 16 pixels, i.e. re-binned 256×256 images, for correction factors of $q_{94} = 1, 2, \dots, 10$, which amount to

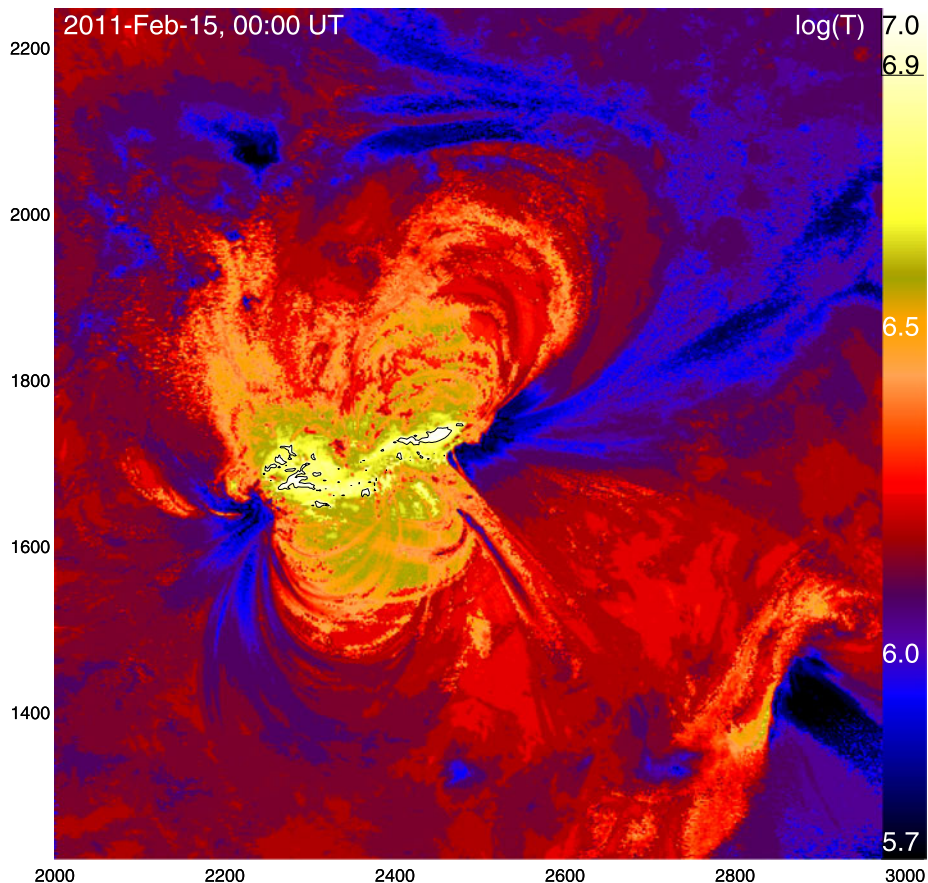


Figure 7 Temperature map of the active region NOAA 11158 (image section $x = 2000\text{--}3024$, $y = 1200\text{--}2224$ pixels) with full spatial resolution (one pixel) in the temperature range $\log(T) = 5.7\text{--}7.0$. The hottest region of $\log(T) \geq 6.9$ ($T \gtrsim 8$ MK) in the core of the active region is marked with a black contour. The logarithmic temperature scale is indicated in the right vertical bar. The units of the axes are given in AIA pixels ($0.6'' \approx 435$ km).

$n = 256^2 \times 10 \approx 5 \times 10^5$ DEM fits. We show the overall goodness of fit as a function of the correction factor [q_{94}] in Figure 6 (right panel) and find a minimum of $\chi^2 = 1.52 \pm 1.40$ at $q_{94} \approx 5$. The effect is even larger when we inspect the number of standard deviations χ_{94} in the 94 Å channel separately, where we infer a correction factor of $q_{94} = 4.9 \pm 3.3$, similar to the former study which has less statistics and mostly near-isothermal loops ($q_{94} = 6.7 \pm 1.7$).

Similar improvements of the response function could also be achieved for two other AIA channels (131 and 335 Å) that are known to be incomplete, as cross-calibrations with SDO/EVE data show (H. Warren, private communication, 2011).

2.6. DEM Peak-Temperature Map of an Active Region

Temperature maps may be calculated first with a coarse resolution for the full Sun (e.g., with 4×4 macropixels in rebinned 1024×1024 full-Sun images as shown in Figure 3), and then with full resolution for a partial area, such as for an active region, which is shown in

Figure 7. This detailed temperature map reveals the spatial distribution of hot, warm, and cool plasma quite distinctly. The hottest zones with temperatures of $T \approx 8-10$ MK (white in Figure 7) are only found in the low-lying core of the active region, while hot loops with $T = 4-8$ MK (yellow in Figure 7) are found in the central volume of the main dipolar structure (oriented in the E–W direction). The large-scale loops that surround the greater area of the central dipole have temperatures in the range of $T \approx 1.5-2.5$ MK (red in Figure 7), and the fan-like structures emerging in E and W directions from the footpoints of the primary dipole are even cooler than $T \lesssim 1.0$ MK (blue in Figure 7). They probably consist of open field lines and cannot trap heated plasma; alternatively, they could represent quasi-separatrix layers according to potential-field source-surface models that may be subject to a peculiar heating function (Schrijver, DeRosa, and Title, 2010). The moss structure, which is the cooler transition region of hot loops, does not notably appear, because it is overwhelmed by the overlying hotter loops that have a higher emission measure. Remember, that the temperature shown here in each pixel corresponds to the peak of the DEM distribution for a given line of sight. In summary, such a detailed temperature map presents the entire temperature range in a less convoluted way than can be gathered from the six different filters with mixed temperature sensitivities.

In principle, temperature maps can also be produced during flares, but instrumental effects, such as the diffraction pattern of the brightest flare kernels and pixel bleeding during flare peak times, produce unwelcome artifacts.

2.7. Peak Emission Measure Map of an Active Region

The peak emission-measure map [$EM_p(x, y)$] is shown in Figure 8, corresponding to the peak-temperature map [$T_p(x, y)$] shown in Figure 7. Be aware that these two maps represent the information of the six coronal AIA filters in a synthesized way, by representing the full DEM distribution in each pixel with an approximation that characterizes the peak of the DEM distribution by a Gaussian function, quantified with the peak emission measure [$EM_p(x, y)$] at the peak temperature [$T_p(x, y)$]. Thus, although a single temperature value [$T_p(x, y)$] is assigned to each image pixel [x, y], the temperature map does not imply that the plasma is isothermal in any location [x, y] (or along the corresponding line of sight), but it represents only the most dominant temperature, in the sense that this temperature characterizes the plasma with the highest emission measure along this line of sight.

Inspecting the fine structure of the DEM peak emission measure map in Figure 8, we notice some coarse graininess in high-temperature zones, similar to the peak-temperature map (Figure 7), which is an intrinsic property of the relative sensitivity of hot and cool filters. The 171 and 193 Å filters with a peak sensitivity in the temperature range of $T \approx 1-2$ MK have the highest sensitivity of the AIA instrument, recording typically ≈ 1000 DN s⁻¹ in active regions, while the 94 Å filter is sensitive to the hottest temperatures [$T \approx 5-10$ MK], but has the lowest intensity of ≈ 10 DN s⁻¹ in active regions (for the nominal exposure times of $t_{\text{exp}} \approx 2-3$ seconds). Nevertheless, the peak emission-measure map (Figure 8) shows us at one glance where most of the plasma mass is concentrated, regardless of its temperature.

2.8. DEM Distribution of an Active Region

Our automated tool that performs forward fitting of single-Gaussian DEM distributions infers a peak emission measure [$EM_p(x, y)$], peak DEM temperature [$T_p(x, y)$], and temperature width [$\sigma_T(x, y)$] for every pixel. Assuming that the single-Gaussian model is an

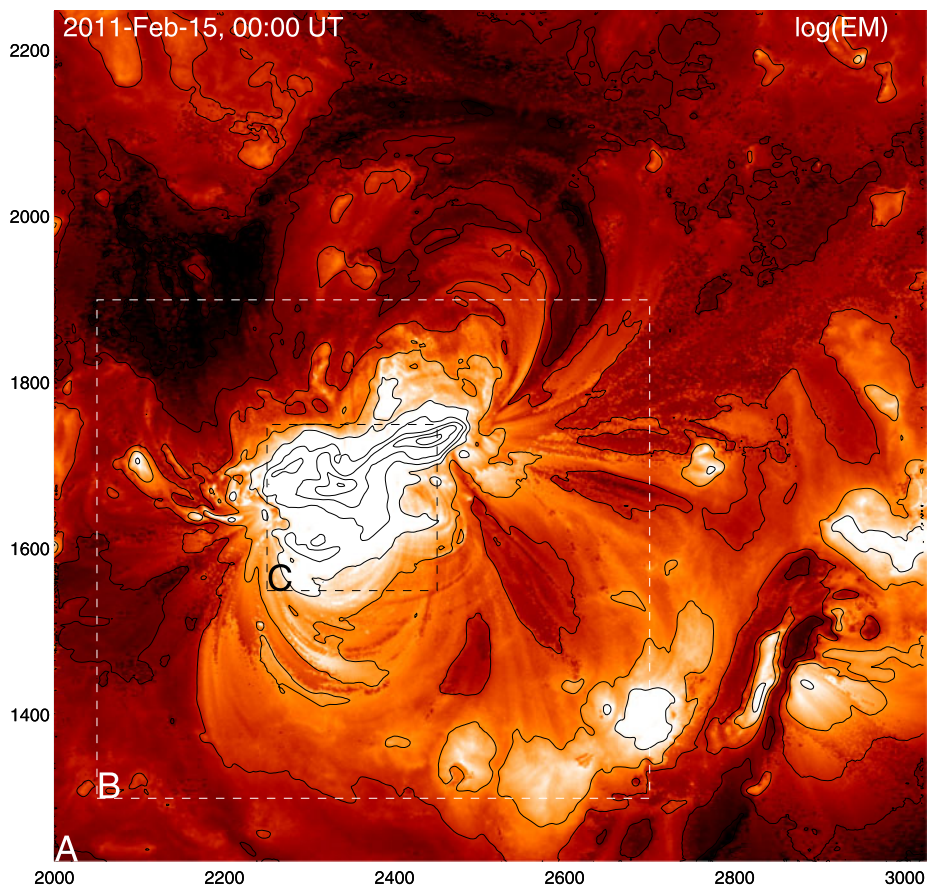


Figure 8 Peak emission-measure map [$EM_p(x, y)$] corresponding to the DEM peak-temperature map [$T_p(x, y)$] shown in Figure 7. The color scale represents the logarithmic emission measure, and the (smoothed) contour levels are at $EM = 10^{19}, \dots, 10^{23} \text{ cm}^5 \text{ K}^{-1}$ with increments by factors of two. The box B demarcates the bright loop area, and the box C the core of the active region, for which the emission measures are averaged in Figure 9. The units of the axes are given in AIA pixels ($0.6'' \approx 435 \text{ km}$).

adequate representation of the single-pixel DEMs, we can then also compose the total DEM distribution of an active region by summing the single-pixel DEMs over all pixels (x_i, y_j) in a field of view that encompasses the active region,

$$\frac{dEM_{\text{AR}}(T)}{dT} = \sum_{i,j} \frac{dEM(T, x_i, y_j)}{dT} = EM_{ij} \exp\left(-\frac{[\log(T) - \log(T_{ij})]^2}{2\sigma_{ij}^2}\right). \quad (9)$$

The resulting total DEM of active region NOAA 11158, integrated over the area shown in Figure 8 (labeled with A in Figures 8 and 9), exhibits a main peak at a temperature of $\log(T) \approx 6.2$, and a secondary peak near $\log(T) \approx 6.7$. When we calculate the total DEM integrated over the bright loop area (labeled as B in Figures 8 and 9) we obtain a DEM that has a comparable emission measure at cool and hot temperatures. If we move further inward to the hot core of the active region (labeled C in Figures 8 and 9), we obtain a DEM that

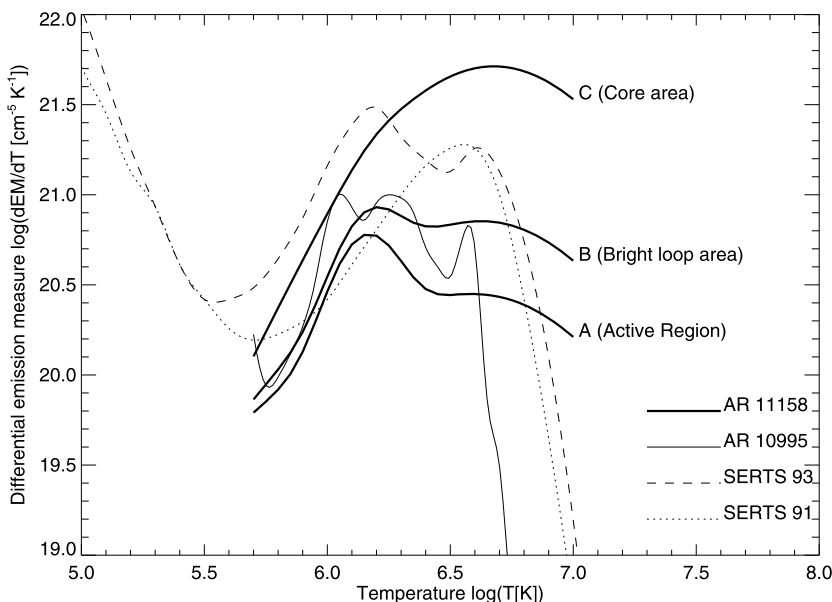


Figure 9 Total differential emission measure [DEM] distribution [dEM/dT] (thick solid curve) of flaring active region NOAA 11158 (15 February 2011), summed from the single-Gaussian DEM fits in each pixel in three different areas: A = entire active region (Figures 7 and 8); B = bright loop area, and C = core of active region (see boxes in Figure 8). The DEMs are compared with those of AR 10995, reconstructed from STEREO observations (Aschwanden et al., 2009), and with two active regions observed in 1991 and 1993 with SERTS (Brosius et al., 1996). Note the order of magnitude higher emission measures and temperatures in the core of the flaring active region, which produced an X2.2 flare 1.5 hours later.

peaks at $\log(T) \approx 6.7$ (or $T \approx 5$ MK). These three areas A, B, and C illustrate how a DEM of an active region is not unique, but strongly depends on the area over which it is averaged.

A comparison with published DEM distributions of other active regions observed with the *Solar EUV Research Telescope and Spectrograph* (SERTS: Brosius et al., 1996), or the *Solar Terrestrial Relations Observatory* (STEREO: Aschwanden et al., 2009), reveals that the flare-producing active region NOAA 11158 has a significantly higher emission measure [$\log(EM) \approx 10^{21.8} \text{ cm}^{-3} \text{ K}^{-1}$] and the peak of the DEM occurs at a higher temperature, when averaged over the core region only; whereas, averaging over a larger active region area [A] yields a lower DEM than that for the other compared active regions.

In order to verify the consistency of the total DEM distribution, we compare the directly observed total fluxes [F_{λ}^{tot}], integrated over the same image area, with the fluxes [F_{λ}^{DEM}] that are predicted by convolving the reconstructed total DEM of the active region (as defined in Equation (9) and shown in Figure 9). The observed and DEM-predicted fluxes for the six AIA filters (Table 1) agree within an accuracy of a few percent (except for the 131 Å channel), which corroborates our method where the total DEM distribution of the active region can be composed from the single-Gaussian DEMs in each pixel. Thus, we are able to reconstruct DEMs over an arbitrary area, which may have a more complicated functional shape than a single-Gaussian function (that is fitted for each pixel), and can be obtained by the superposition of the single-Gaussian DEMs from each contributing pixel. Our DEM distribution reconstructed here is only constrained in the temperature range of $\log(T) = 5.7 - 7.0$.

Table 1 Total fluxes F_{tot} of active region NOAA 11158, fluxes $F_{\text{tot}}^{\text{DEM}}$ predicted from the summed (single-Gaussian) DEM distributions of all pixels, and ratios q_{flux} .

| Wavelength λ | Flux F_{tot} [DN s $^{-1}$] | Flux $F_{\text{tot}}^{\text{DEM}}$ [DN s $^{-1}$] | Ratio |
|----------------------|---------------------------------------|--|-------|
| 131 Å | 8.850×10^6 | 5.207×10^6 | 0.588 |
| 171 Å | 2.056×10^8 | 2.127×10^8 | 1.034 |
| 193 Å | 2.421×10^8 | 2.362×10^8 | 0.976 |
| 211 Å | 8.772×10^7 | 8.912×10^7 | 1.016 |
| 335 Å | 6.932×10^6 | 8.109×10^6 | 1.170 |
| 94 Å | 3.075×10^6 | 3.255×10^6 | 1.058 |

2.9. Automated Loop Detection

We are now proceeding from large-scale coronal structures (such as active regions) to individual fine structures (such as coronal loops), whose electron temperature and density can only be properly measured after an accurate cospatial background flux subtraction. A first requirement of an automated analysis of coronal loops is automated detection. The recently developed *Oriented Coronal CURved Loop Tracing* (OCCULT) code is a numerical code with automated feature extraction, customized for the tracing of coronal loops, which approaches the quality of visual loop perception (Aschwanden, 2010a, 2010b). The OCCULT method is based on oriented-directivity tracing of curvilinear features. However, in contrast to other general feature-extraction algorithms, it is customized to solar EUV and SXR images by taking advantage of the specific property that coronal loops have large curvature radii compared to their widths. The performance of alternative codes has been compared in a benchmark study of Aschwanden *et al.* (2008b), which included the following five numerical codes: *i*) an early oriented-directivity code that uses external information from a magnetic-field extrapolation (Lee, Newman, and Gary, 2004, 2006a); *ii*) a dynamic aperture-based method of solar-loop segmentation (Lee, Newman, and Gary, 2006b); *iii*) an unbiased detection method of curvilinear structures developed by Steger (1996), Raghupathy (2004), and Smith (2005); *iv*) an oriented-directivity code which was a precursor of the OCCULT code; and *v*) a code for ridge detection by automated scaling (Inhester, Feng, and Wiegemann, 2007). More recent developments include *vi*) the detection of elliptical loop geometries using the incremental Hough transform (Sellah and Nasraoui, 2008), *vii*) supervised (neural) learning strategies based on classifiers, such as RIPPER, Multi-Layer Perceptron, or Adaboost (Durak, Nasraoui, and Schmelz, 2010), and *viii*) a wavelet transform modulus maxima method (McAteer *et al.*, 2010). A number of these codes employ general pattern-recognition methods, such as image segmentation, Radon transform, wavelet transform, Hough transform, ridgelet detection, or neural learning. Others are geared more toward specific patterns of coronal loops, which follow the magnetic field and thus have elliptical shapes, large curvature radii, and Gaussian cross-sectional profiles, and can be traced with oriented-directivity methods.

Here we apply the OCCULT loop-tracing code (Aschwanden, 2010a, 2010b) for the first time to AIA images. A set of highpass-filtered images in the six coronal wavelengths is shown in Figure 10, with the automated loop tracings overlaid. We used the following control parameters for the OCCULT code: $r_{\min} = 25$ pixels minimum curvature radius of loops, $w = 3$ pixels for highpass filtering to enhance loop structures, $n_{\text{sig}} = 0.5$ standard deviations as the flux threshold level to trace loop structures, $q_{\text{fill}} = 0.35$ minimum filling factor (which quantifies the minimum tolerance for intermittent loop structures), and $L_{\min} = 15$ pixels for the minimum acceptable loop length. In addition, we reduced the stepping parameter from $N_{\text{step}} = 3 + 2w$ in the original code to $N_{\text{step}} = 1$, which produced slightly improved results.

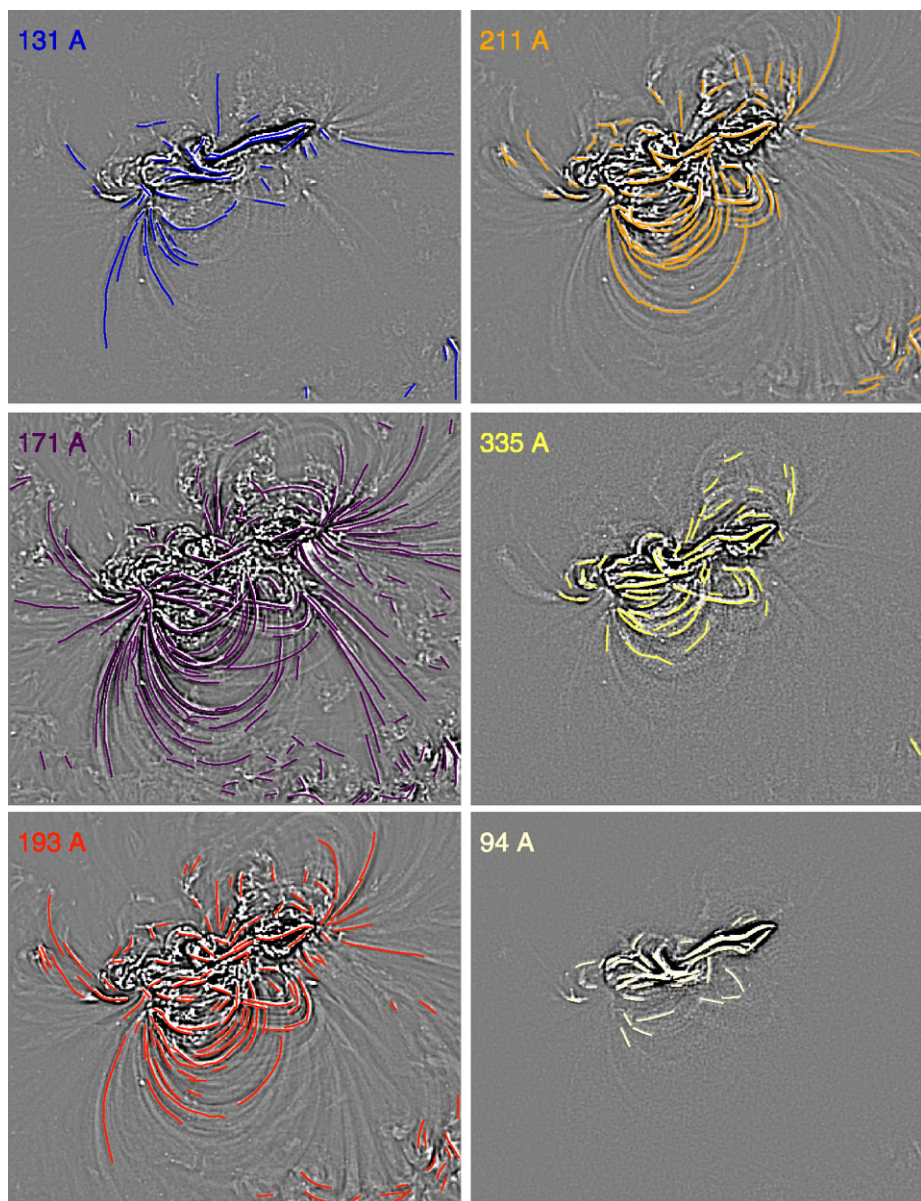


Figure 10 Automated loop tracings in the six AIA filters, overlaid on highpass-filtered images that were used to enhance and trace individual loops. The partial image covers the core of the active region as shown in Figures 7 and 8, including the pixel ranges of $x = 2050 - 2700$ and ($y = 1300 - 1900$) of the original 4096×4096 image (Figure 1). The AIA pixel size is $0.6'' \approx 435$ km, and the field of view is 283 Mm \times 261 Mm.

The tracings shown in Figure 10 prove that the chosen flux threshold of $n_{\text{sig}} = 0.5$ still suppresses the detection of noise structures outside of the active region, especially in the 94 Å filter. The combined loop tracings in all six wavelengths are shown in Figure 11, color-coded

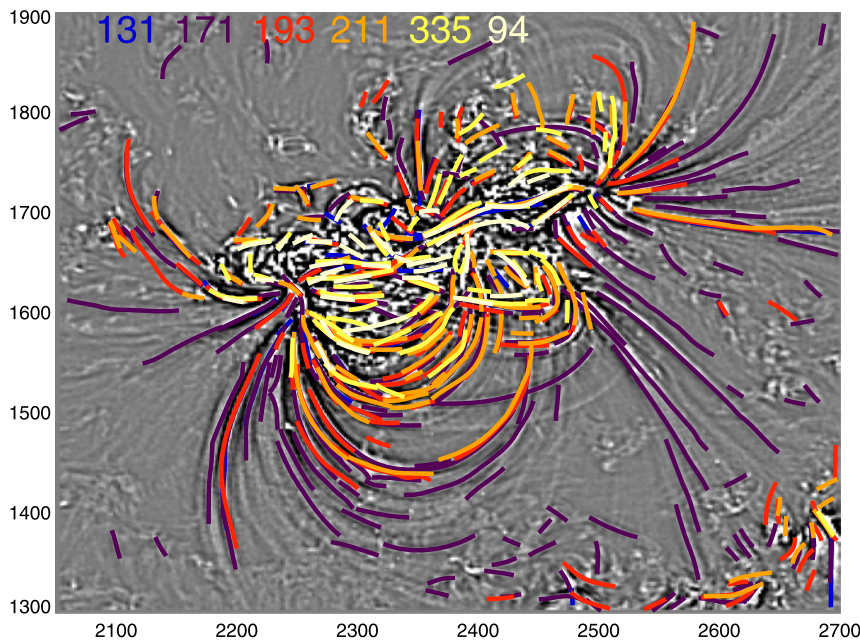


Figure 11 Overlay of automated loop tracings in all six AIA filters. The color code of the wavelengths is indicated at the top of the image. The partial image covers the area B shown in Figure 8. The field of view is 283 Mm \times 261 Mm.

for each filter. Note that hot loops detected in the 335 and 94 Å filters are predominantly located in the core of the active region, while cooler loops detected in 171 Å skirt the outer zones and higher altitudes of the active region. The numbers of automatically detected loop segments in the various wavelengths are: 49 in 131 Å, 190 in 171 Å, 128 in 193 Å, 104 in 211 Å, 62 in 335 Å, and 37 in 94 Å, amounting to a total of 570 loop segments, which also include some overlapping or cospatial segments in different wavelengths.

One caveat of independent loop detection in different wavelength filters is that only segments with a limited temperature variation ($\Delta \log(T) \approx 0.3$) can be traced coherently in one single filter. A consequence is that long loop segments detected in one single filter have statistically a smoother longitudinal temperature gradient than shorter segments. However, this should not affect the cross-sectional temperature analysis.

2.10. Automated Temperature Analysis of Coronal Loops

The automated loop-detection tool (OCCULT), which we described in Section 2.9, in combination with the automated DEM fitting method (described in Section 2.4 for total fluxes), gives us for the first time an unbiased, objective, and automated method to determine emission measures [$EM(s, i_{loop})$] and temperatures [$T(s, i_{loop})$] of loop segments [i_{loop}] as a function of the loop length coordinate [s]. In the optimum case, a complete loop can be traced from one to the other footpoint, $0 \leq s \leq L$, over the entire loop length [L], but generally only a partial segment in the range $[s_1, s_2]$ can be continuously traced ($0 \leq s_1 \leq s \leq s_2 \leq L$), due to interfering secondary structures (e.g., moss or crossing loops along the same line of sight) or weak emission near the loop top. Also, some segments may belong to open-ended loops or fans, rather than to closed loops. Nevertheless, the loop tracings provide the parallel

direction of the loop axis, and an objective background can be subtracted by interpolating the loop edges in a perpendicular direction, which can be self-consistently (cospatially) performed in all wavelength filters in a fully automated way. A convenient loop background definition is a Gaussian cross-sectional fit [$G_\lambda(x)$] in the direction perpendicular to the loop [x] at a particular loop segment position [s],

$$G_\lambda(x) = F_\lambda^{\text{loop}} \exp\left(-\frac{(x - x_0)^2}{2\sigma_w^2}\right) + B_0 + B_1(x - x_0), \quad (10)$$

where x_0 represents the loop midpoint position, and a cospatial linear background flux profile is defined by

$$B_\lambda(x) = B_0 + B_1(x - x_0), \quad (11)$$

as has been used for previous temperature analyses of coronal loops observed with the *Transition Region and Coronal Explorer* (TRACE: Aschwanden and Nightingale, 2005) or SDO/AIA (Aschwanden and Boerner, 2011). The background-subtracted fluxes [F_λ^{loop}] in the six different wavelength filters can then be used for a DEM forward fit (Equation (4)), for instance, parameterized with a Gaussian DEM function [$dEM(T)/dT$: Equation (5)] that yields the loop DEM peak emission measure [EM^{loop}], loop DEM peak temperature [T^{loop}], and Gaussian temperature width [σ_T^{loop}]. The latter parameter, *i.e.* the Gaussian temperature width, contains information on whether the loop has an isothermal or multithermal characteristics.

We run an automated program that: *i*) subdivides the loop segments into elemental length units of $\Delta s = 5$ pixels, *ii*) averages the loop cross-sectional profiles [$F_\lambda^{\text{obs}}(x)$] along this length Δs within a width of $n_w = 25$ pixels (≈ 10 Mm) across the loop, *iii*) determines a Gaussian cross-sectional profile [$G_\lambda(x)$ (Equation (9))] with linear background profile [$B_\lambda(x)$ (Equation (11)) in all six AIA filters, *iv*) performs a single-Gaussian DEM fit, determines the emission measure [$EM_{\text{loop}}(s)$], temperature [$T_{\text{loop}}(s)$], and temperature width [σ_T^{loop}], and infers the electron density [$n_e^{\text{loop}}(s)$] using the Gaussian loop width $w(s) = 2\sqrt{2 \ln 2} \sigma_w(s) \approx 2.35 \sigma_w(s)$,

$$n_e^{\text{loop}}(s) = \sqrt{\frac{EM^{\text{loop}}(s)}{w(s)}}, \quad (12)$$

assuming a filling factor of unity inside the loop cross section.

The automated DEM-code performs this analysis for all 570 automatically detected loop segments (Figures 10 and 11), which are broken down into 3837 subsegments with a length of $\Delta s = 5$ pixels. We show the results of three loops (out of the 570 loops) in Figures 12, 13, and 14. Figure 12 shows the results of loop number 171/68, which was automatically detected in the 171 wavelength: the local image with the tracing box (Figure 12, top right), the subimages of the tracing box stretched out parallel to the loop axis in all six filters (Figure 12, bottom left), the cross-sectional flux profiles [$F_\lambda(x)$] along the loop (Figure 12, top left), and the single-Gaussian DEM best-fit parameters: the electron temperature [$T_e(s)$] and Gaussian temperature width [$\sigma_T(s)$] (indicated as error bars for each DEM peak-temperature value), the electron density [$n_e(s)$], the loop width [$w(s)$], and the goodness of fit [$\chi^2(s)$] (Figure 12, panels on right side). Note that the loop is best visible in the 171 Å filter, and with somewhat less contrast in the 131 Å filter, while there is no corresponding cospatial tracing with equal width detectable in the other channels, which is consistent with the inferred temperature of $\log(T_e) = 5.8 \pm 0.2$. Note also that the $\chi^2 = 1.15 \pm 0.51$ indicates an acceptable DEM fit for most positions along the loop.

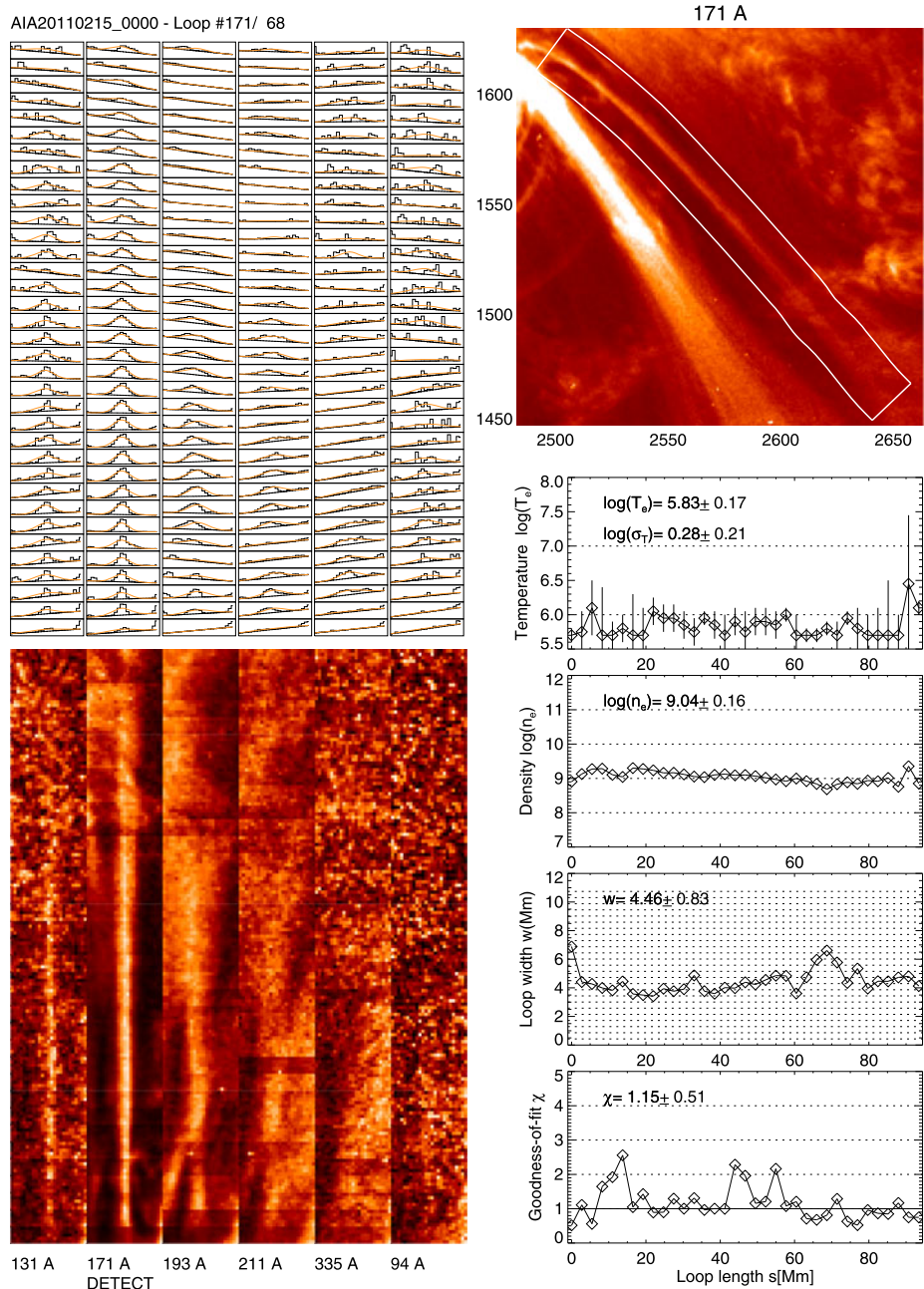


Figure 12 Example of automated emission-measure and temperature analysis of loop number 171/68, which was detected in the 171 Å filter. A partial image of the automated loop tracing is shown in the top right panel; the stretched-out loop segments are shown in the bottom left panels. The cross-sectional flux profiles are shown in the top left panels. The best-fit values of the DEM peak temperature [$T_e(s)$], Gaussian temperature width [$\sigma_T(s)$] (error bars in temperature plot), the electron densities [$n_e(s)$], loop widths [$w(s)$], and goodness of fit [$\chi^2(s)$] of the single-Gaussian DEM fits are shown in the right-hand panels.

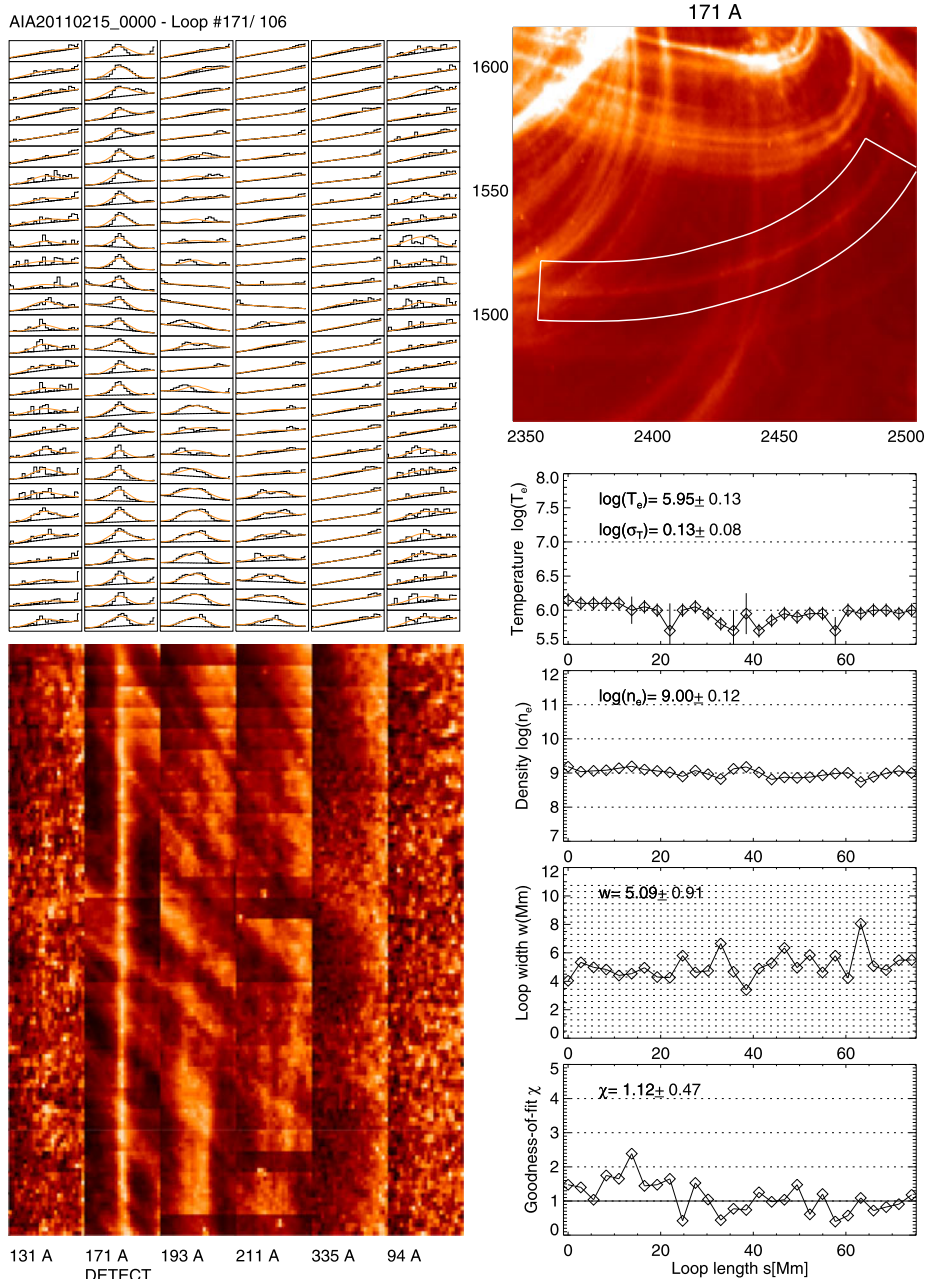


Figure 13 Example of a loop that is intersected by a number of other loops in the diagonal direction. Note that the automated temperature, density, and width measurements are robust and consistent along the loop, although the background subtraction is hampered by diagonally crossing loops. Layout similar to Figure 12, containing loop cross-sectional profiles (top left), stretched-out loop segments (bottom left), subimage encompassing analyzed loop (top right), and parameter functions along the loop (bottom right panels).

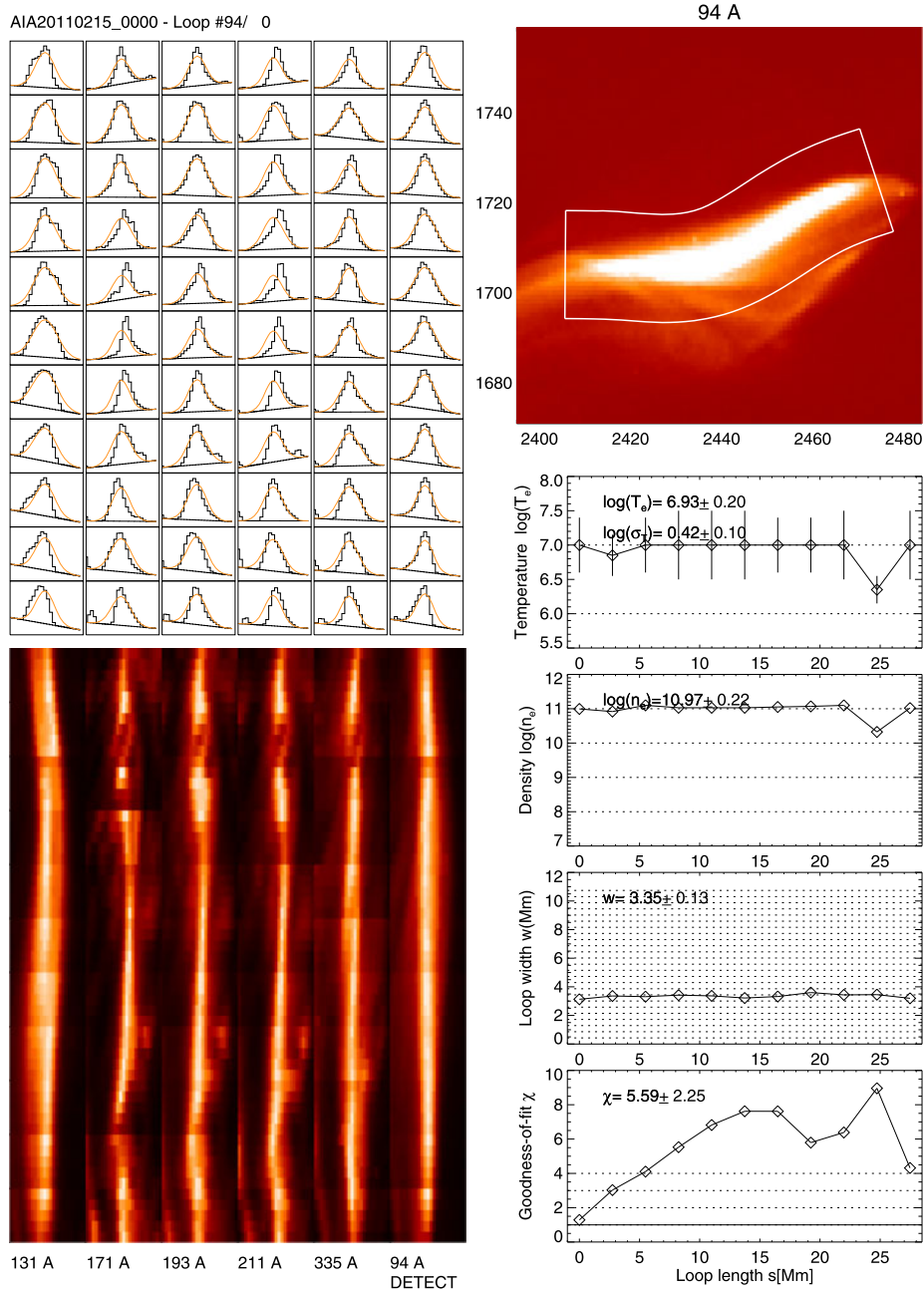


Figure 14 Example of a very hot loop (or filament) detected in 94 Å, in the core of the active region, which shows up prominently in all six filters. This apparently multithermal loop exhibits a large Gaussian temperature width of $\sigma_T = 0.42 \pm 0.10$, but cannot be fitted well with a single-Gaussian DEM, as the $\chi^2 = 5.6 \pm 2.3$ indicates.

Figure 13 shows the automated DEM analysis of another loop (number 171/106), also detected in the 171 Å filter, but oriented so that a large number of secondary loops intersect in the fore- or background at some diagonal angle (Figure 13, bottom left). This example demonstrates the robustness of our algorithm, which is able to trace the loop without derailing in diagonal directions, and to determine a suitable local background at every loop position, with a consistent temperature [$T_e(s)$], density [$n_e(s)$], and width profile [$w(s)$] along the loop, with an acceptable goodness of fit, $\chi^2 = 1.1 \pm 0.5$. The analyzed loop is close to isothermal, with $\log(\sigma_T) = 0.13 \pm 0.08$.

In Figure 14 we show one of the rare examples that turned out to be multithermal, loop number 94/0; it was traced in the 94 Å filter, but is clearly detectable in all six filters. The best single-Gaussian fit yields a relatively high temperature of $\log(T_e) = 6.93 \pm 0.20$ (at the upper limit of our valid DEM range, $\log(T_e) \leq 10^7$), a Gaussian temperature width of $\log(\sigma_T) = 0.42 \pm 0.10$, an electron density of $\log(n_e) = 10.97 \pm 0.22$, and a loop width of $w = 3.35 \pm 0.13$ Mm. However, this loop cannot be fitted well with a single-Gaussian DEM, as the $\chi^2 = 5.6 \pm 2.3$ indicates, not even with a broad Gaussian, probably requiring a multi-peaked DEM distribution function. This structure is located in the core of the active region and is filled with plasma that corresponds to flare densities. It might represent a heated filament rather than a coronal loop.

Statistics of the automated DEM fits at 3837 locations in the 570 traced loop segments in AR 11158 are provided in Figure 15. The success of the automated DEM fits can be judged from the goodness-of-fit statistics, which yields a distribution of $\chi^2 = 1.50 \pm 1.02$ (Figure 15, top right), with 2892 cases (75%) satisfying an acceptable fit (of $\chi^2 < 2.0$). The distribution of loop temperatures exhibits a peak at $\log(T_e) \lesssim 5.7$ and near $\log(T_e) = 6.0 - 6.2$, but loop temperatures are measured in the entire range of $\log(T_e) = 5.7 - 7.0$. The electron densities peak around $n_e = 10^{9.33 \pm 0.44} \text{ cm}^{-3}$, which agrees well with earlier statistics (e.g., $n_e = 10^{8.96 \pm 0.18} \text{ cm}^{-3}$ in 17 908 loop positions measured with TRACE; Aschwanden and Nightingale (2005)). A scatter-plot of the electron density with temperature is shown in Figure 15 (top left), which we will discuss in the next section in terms of loop scaling laws.

The Gaussian width of the DEM temperature distribution is $\sigma_T = 0.24 \pm 0.20$ (Figure 15, bottom left), but the distribution is not symmetrical. It peaks at the temperature resolution limit of $\sigma_T \gtrsim 0.1$, which means that most loops are close to isothermal. The loop width distribution peaks at $w = 5.10 \pm 0.47$ Mm (about nine AIA pixels), which is about five times the spatial resolution of the instrument and is mostly determined by the applied highpass filter. We used a smoothing width of nine pixels in the automated tracing of loops, which detects loops with comparable widths most efficiently.

Regarding the functional shape of DEMs of single coronal loops, the single-Gaussian DEM parameterization, as used in the automated loop DEM analysis in Section 2.10, turns out to be a suitable approximation in 66% of loops. A double-Gaussian approximation is required in 19%, and more complex DEM distribution functions are needed in the remaining 15%, according to a recent DEM modeling study of 100 loop cross sections observed with AIA (Aschwanden and Boerner, 2011).

2.11. Tests of the RTV Scaling Law

From the large statistics of $\approx 10^6$ DEM characterizations in a 1024×1024 (rebinned) image we can study the scaling law of emission measure [EM] *versus* temperature [T]. For a hydrostatic equilibrium and energy balance between heating and cooling, Rosner, Tucker, and Vaiana (1978) derived a scaling law between the loop maximum temperature [T_e], pressure

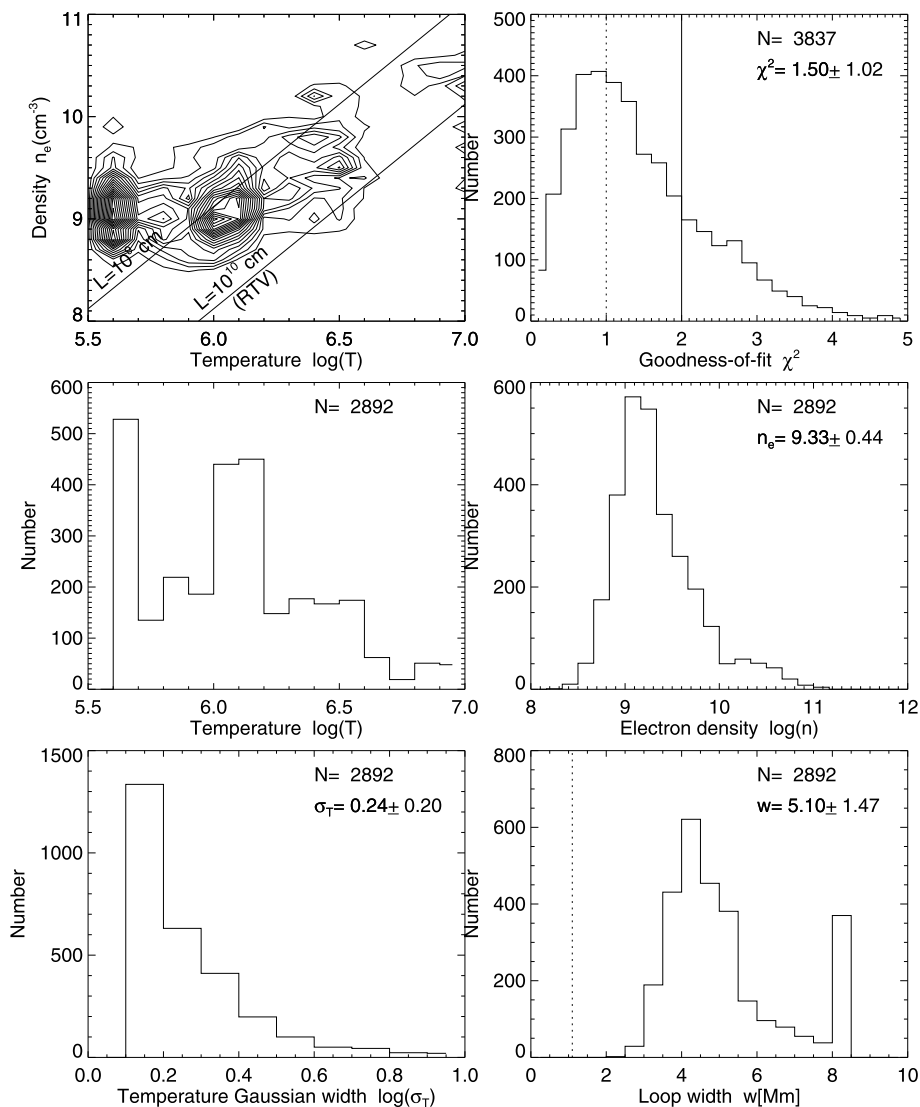


Figure 15 Statistics of physical parameters inferred from 3837 automatically detected loops in AR 11158: contour plot of electron density n_e vs. electron temperature distribution (top left), with the RTV scaling law indicated for $L = 10$ Mm and $L = 100$ Mm (straight line); distributions of electron temperatures (middle left), Gaussian temperature widths σ_T (bottom left), goodness of fit χ^2 of single-Gaussian fits (top right), electron densities (middle right), and loop widths (bottom right).

[p], and loop length [L], i.e., $T_e^3 \propto pL$, which together with the pressure for an ideal gas [$p = 2n_e k_B T_e$] yields a relationship between the electron density [n_e] and temperature [T_e]:

$$n_e \propto \frac{T_e^2}{L}. \quad (13)$$

In Figure 15 we plot the inferred loop density [n_e] *versus* the peak temperature [T_e] and indeed find that most of the datapoints fall into the diagonal band predicted by the RTV law for loops with lengths of $10^9 \text{ cm} \leq L \leq 10^{10} \text{ cm}$, at least for the hotter regime of $\log(T) \approx 6.4 - 7.0$, which corresponds to the temperature regime ($T \approx 2.5 - 10 \text{ MK}$) of soft X-rays. This relationship has also been confirmed for combined solar and stellar flare data (Aschwanden, Stern, and Güdel, 2008). In the lower temperature regime $\log(T) \approx 5.7 - 6.4$ ($T \approx 0.5 - 2.5 \text{ MK}$), in contrast, the observed emission measures are higher than expected from the RTV law, which is known to result from a deviation from the energy balance between heating and cooling, which leads to a relative over-density in cooling loops (Serio *et al.*, 1981; Lenz *et al.*, 1999; Aschwanden *et al.*, 1999). The same trend of $n_e \propto T_e^2$, which corresponds to $EM_p \propto T_e^4$ for a fixed loop length [L], is also apparent for arbitrary pixels as shown over the entire active region in Figure 5, because every pixel samples the emission measure [EM] and temperature [T_e] of the dominant loop that intersects a particular pixel. The excess of datapoints at the lower boundary of the temperature range at $\log(T_e) = 5.6$ is likely to be caused by the artificial limit set in the fitting procedure.

3. Summary and Outlook

In this article we describe recent progress in the SDO/AIA data analysis, which is an ongoing project and is likely to develop further over the upcoming years of the mission. Focusing on coronal loops, we conducted an initial study on the temperature and emission measure of ten individual loops observed at ten different times (Aschwanden and Boerner, 2011), which helped to establish the efficiency and accuracy of various differential emission measure [DEM] reconstruction methods. Based on this experience, we developed the AIA data analysis further to the point at which it can be run in an automated mode, which includes the following analysis tools:

- i) Coalignment test between different AIA wavelength filters based on the steepest flux gradients at the EUV limb.
- ii) Self-calibration of the AIA instrumental-response functions by large statistics of DEM χ^2 fits with empirically modified instrumental temperature-response functions.
- iii) DEM distribution peak-temperature maps [$T_p(x, y)$] and peak emission-measure maps [$EM_p(x, y)$].
- iv) Synthesized DEM distributions [$dEM(T, x, y)/dT$] integrated over arbitrary areas of active regions or the solar corona.
- v) Automated tracing of coronal loop coordinates [$x(s), y(s)$] in all wavelength filters.
- vi) Automated DEM fits to background-subtracted loop fluxes [$F_\lambda(s)$] with measurements of the temperature [T_e], temperature width [σ_T], emission measure [EM], electron density [n_e], and loop width [w].

These analysis tools are currently implemented in the Solar Software (SSW). A user guide will be available at the first author's software homepage (<http://www.lmsal.com/~aschwand/software>) or the SDO documentation website (<http://www.lmsal.com/sdodocs/>).

Scientific applications of these automated analysis tools include (but are not limited to):

- i) Chromospheric height measurements.
- ii) Emission measure *versus* temperature scaling laws (e.g., the RTV law $EM \propto T_e^4$) and validity tests in different temperature ranges.
- iii) Functional shape of the DEM distribution, which can be compared with hydrostatic and hydrodynamic coronal models (e.g., see Section 3.10 in Aschwanden, 2004).

- iv) Physical parameters of loops [$EM(s)$, $T_e(s)$, $n_e(s)$, $w(s)$] as a function of the loop length coordinate [s], which can be used for hydrostatic and hydrodynamic modeling, as well as for coronal seismology and coronal heating models.
- v) The temperature width [σ_T] of the DEM peak, which yields an important diagnostic on the isothermality or multithermality of coronal loops, which in turn can be used as a test criterion to discriminate between various coronal heating models.

For hydrostatic and hydrodynamic loop modeling, the full loop length [L] of a loop is the next important parameter, and it cannot be determined in most cases with current automated loop-tracing codes. For instance, the RTV law is expressed in terms of temperature, pressure, and loop length, and thus it requires a measurement of the loop length [L]. In fortunate cases the loop footpoint and apex locations can be determined with some certainty by visual judgment, which can provide the full loop length in those cases. Alternatively, the full loop length can be determined by means of stereoscopy (e.g., Aschwanden *et al.*, 2008b, 2008c, 2009). However, in the absence of stereoscopic data, we anticipate a reconstruction of the approximate three-dimensional geometry of full loops with the aid of magnetic modeling, e.g. by automated decomposition of magnetograms into unipolar or bipolar magnetic domains and forward fitting of adjustable magnetic potential-field models (e.g., Aschwanden and Sandman, 2010; Sandman and Aschwanden, 2011), which could lead to an automated full-loop reconstruction. The physics of coronal loops cannot be fully understood without a knowledge of the magnetic field, especially for applications of coronal seismology and tests of coronal heating models (e.g., see Section 9 in Aschwanden, 2004).

A further development that we anticipate is the automated tracking of loops, which can be expanded from our automated loop-detection code, also taking the solar rotation into account. Once we are able to automatically track a well-defined coronal loop during its entire lifetime, starting from the initial heating phase through its evolution to the maximum temperature and peak density time, with subsequent cooling phases, dominated first by conductive cooling and later by radiative cooling, we will have a sufficient set of observables ready for hydrodynamic modeling and the determination of the spatial and temporal heating function, which one hopes will lead to the solution of the coronal heating problem.

Acknowledgements The authors acknowledge helpful and constructive discussions with Harry Warren, Paola Testa, and Mark Weber during an AIA meeting on instrumental-response functions and DEM inversions, held in Palo Alto in February 2011. This work is partially supported by NASA under contract NNG04EA00C for the SDO/AIA instrument. SDO data and images are courtesy of NASA/SDO and the AIA science team.

References

- Aschwanden, M.J.: 2004, *Physics of the Solar Corona – An Introduction*, Springer/Praxis, New York. ISBN 3-540-22321-5.
- Aschwanden, M.J.: 2010a, *Solar Phys.* **262**, 235.
- Aschwanden, M.J.: 2010b, *Solar Phys.* **262**, 399.
- Aschwanden, M.J., Acton, L.W.: 2001, *Astrophys. J.* **550**, 475.
- Aschwanden, M.J., Boerner, P.: 2011, *Astrophys. J.* **732**, 81.
- Aschwanden, M.J., Nightingale, R.: 2005, *Astrophys. J.* **633**, 499.
- Aschwanden, M.J., Sandman, A.W.: 2010, *Astron. J.* **140**, 723.
- Aschwanden, M.J., Stern, R.A., Güdel, M.: 2008, *Astrophys. J.* **672**, 659.
- Aschwanden, M.J., Newmark, J.S., Delaboudinière, J.P., Neupert, W.M., Klimchuk, J.A., Gary, G.A., Portier-Fornazzi, F., Zucker, A.: 1999, *Astrophys. J.* **515**, 842.
- Aschwanden, M.J., Lee, J.K., Gary, G.A., Smith, M., Inhester, B.: 2008a, *Solar Phys.* **248**, 359.
- Aschwanden, M.J., Nitta, N.V., Wuelser, J.P., Lemen, J.R.: 2008b, *Astrophys. J.* **680**, 1477.

- Aschwanden, M.J., Wuelser, J.P., Nitta, N., Lemen, J.: 2008c, *Astrophys. J.* **679**, 827.
- Aschwanden, M.J., Wuelser, J.P., Nitta, N., Lemen, J., Sandman, A.: 2009, *Astrophys. J.* **695**, 12.
- Boerner, P., Edwards, C., Lemen, J., Rausch, A., Schrijver, C., Shine, R., Shing, L., Stern, R., Tarbell, T., Title, A., Wolfson, C.J.: 2011, *Solar Phys.* doi:[10.1007/s11207-011-9804-8](https://doi.org/10.1007/s11207-011-9804-8).
- Brosius, J.W., Davila, J.M., Thomas, R.J., Monsignori-Fossi, B.C.: 1996, *Astrophys. J. Suppl.* **106**, 143.
- Durak, N., Nasraoui, O., Schmelz, J.: 2010, *Solar Phys.* **264**, 383.
- Fludra, A., Sylwester, J.: 1986, *Solar Phys.* **105**, 323.
- Inhester, B., Feng, L., Wiegelmann, T.: 2007, *Solar Phys.* **248**, 379.
- Ireland, J., Young, C.A. (eds.): 2010, *Solar Phys.* **262**. <http://www.springerlink.com/content/0038-0938/262/2/>.
- Kashyap, V., Drake, J.J.: 1998, *Astrophys. J.* **503**, 450.
- Lee, J.K., Newman, T.S., Gary, G.A.: 2004, In: Kittler, J., Petrou, M., Nixon, M.S. (eds.) *Proc. 17th International Conference on Pattern Recognition (ICPR)*, IEEE-CS, Washington, 315. doi:[10.1109/ICPR.2004.1333766](https://doi.org/10.1109/ICPR.2004.1333766).
- Lee, J.K., Newman, T.S., Gary, G.A.: 2006a, *Pattern Recognit.* **39**, 246.
- Lee, J.K., Newman, T.S., Gary, G.A.: 2006b, In: *Proc. 7th IEEE SSIAI*, Denver, CO, 91.
- Lemen, J.R., Title, A.M., Akin, D.J., Boerner, P.F., Chou, C., Drake, J.F., Duncan, D.W., Edwards, C.G., Friedlaender, F.M., Heyman, G.F., Hurlburt, N.E., Katz, N.L., Kushner, G.D., Levay, M., Lindgren, R.W., Mathur, D.P., McFeaters, E.L., Mitchell, S., Rehse, R.A., Schrijver, C.J., Springer, L.A., Stern, R.A., Tarbell, T.D., Wuelser, J.-P., Wolfson, C.J., Yanari, C.: 2011, *Solar Phys.* doi:[10.1007/s11207-011-9776-8](https://doi.org/10.1007/s11207-011-9776-8).
- Lenz, D.D., DeLuca, E.E., Golub, L., Rosner, R., Bookbinder, J.A.: 1999, *Astrophys. J. Lett.* **517**, L155.
- McAteer, R.T., Kestener, P., Arneodo, A., Khalil, A.: 2010, *Solar Phys.* **363**, 387.
- Raghupathy, K.: 2004, Ph.D. Thesis, Cornell University.
- Rosner, R., Tucker, W.H., Vaiana, G.S.: 1978, *Astrophys. J.* **220**, 643.
- Sandman, A.W., Aschwanden, M.J.: 2011, *Solar Phys.* **270**, 503. doi:[10.1007/s11207-011-9782-x](https://doi.org/10.1007/s11207-011-9782-x).
- Schrijver, C.J., DeRosa, M.L., Title, A.M.: 2010, *Astrophys. J.* **719**, 1083.
- Sellah, S., Nasraoui, O.: 2008, In: *Tools with Artificial Intelligence, ICTAI'08, 20th IEEE Internat. Conf.* **2**, 45. doi:[10.1109/ICTAI.2008.147](https://doi.org/10.1109/ICTAI.2008.147).
- Serio, S., Peres, G., Vaiana, G.S., Golub, L., Rosner, R.: 1981, *Astrophys. J.* **243**, 288.
- Smith, M.: 2005, <http://www.mssl.ucl.ac.uk/twiki/bin/view/SDO/LoopRecognition>.
- Steger, L.H.: 1996, An unbiased detector of curvilinear structures, Technical Report FGBV-96-03, Forschungsgruppe Bildverstehen (FG BV), Informatik IX, Technische Universität München, Germany.
- Zhang, J., White, S.M., Kundu, M.R.: 1998, *Astrophys. J. Lett.* **504**, L127.